Electronic supplementary materials

For: https://doi.org/10.1631/jzus.A2200551

Experimental and theoretical analysis of a hybrid vibration energy harvester with integrated piezoelectric and electromagnetic interaction

Shifan HUANG, Weihao LUO, Zongming ZHU, Zhenlong XU, Ban WANG, Maoying ZHOU, Huawei QIN

School of Mechanical Engineering, Hangzhou Dianzi University, Hangzhou 310018, China

S1 Lumped-parameter model of the HEHPE

For the sake of theoretical analysis, equivalent lumped-parameter representations of the studied HEHPE are established and shown in Fig. S1. The four connection topologies shown in Fig. S2 in the main manuscript are represented in Figs. S1a–1d, respectively. Some simplifications have been made in this process. Firstly, the base excitation is thought to be small and thus seen as infinitesimal in the theoretical analysis. In this sense, the piezoelectric beam model is readily linearized. Secondly, the electromechanical resonance, electrical resonance, and mechanical resonance in the HEHPE are thought to be isolated from each other. As a result, we can describe the three parts separately in the theoretical model, without loss essence of the problem. Thirdly but not the least important, the attached electromagnetic part to the free end of the piezoelectric part is assumed to be rigid and the connection between them is assumed perfect without damping.

Since the studied HEHPE is intended for low-frequency applications, only the first-order reduced order model of the piezoelectric part is considered here. In Fig. S1, C_m, K, and M_{ef} are the equivalent mechanical damping, equivalent stiffness and equivalent mass of the piezoelectric part respectively. C_d, C_e, and m_e are the equivalent mechanical damping, equivalent electromagnetic damping and equivalent mass of the electromagnetic part respectively. F_{mag} is the nonlinear magnetic force applied to the moving magnet by the two fixed magnets. $z(t)$ and $y(t)$ are the deflection of the piezoelectric cantilever beam and the displacement of the moving magnet respectively. V_p is the voltage across the piezoelectric plates in the piezoelectric

cantilever beam. i_e is the induced current in the induction coil, and i is the current passing through the resistance load R_{load} when the piezoelectric part and the electromagnetic part are electrically connected in serial. $Asin(wt)$ is the excitation acceleration with A being the amplitude and *w* being the angular frequency.

As shown in Fig. S1a, the HEHPE with connection topology 1 corresponds to classical piezoelectric energy harvesters with end mass. With this in mind, lumped-parameter model of the HEHPE in connection topology 1 is listed as follows:

$$\begin{aligned} M_{ef}\ddot{z} + C_m\dot{z} + Kz + \theta V_p &= -M_{ef}A\sin(wt) \\ C_p\dot{V}_p + \frac{V_p}{2R_p} - \theta\dot{z} &= 0 \end{aligned} \tag{S1}$$

where θ is the electromechanical coupling coefficient of the piezoelectric part, C_p is the equivalent capacitance of the piezoelectric part, and over dots represent the derivatives with respect to time.

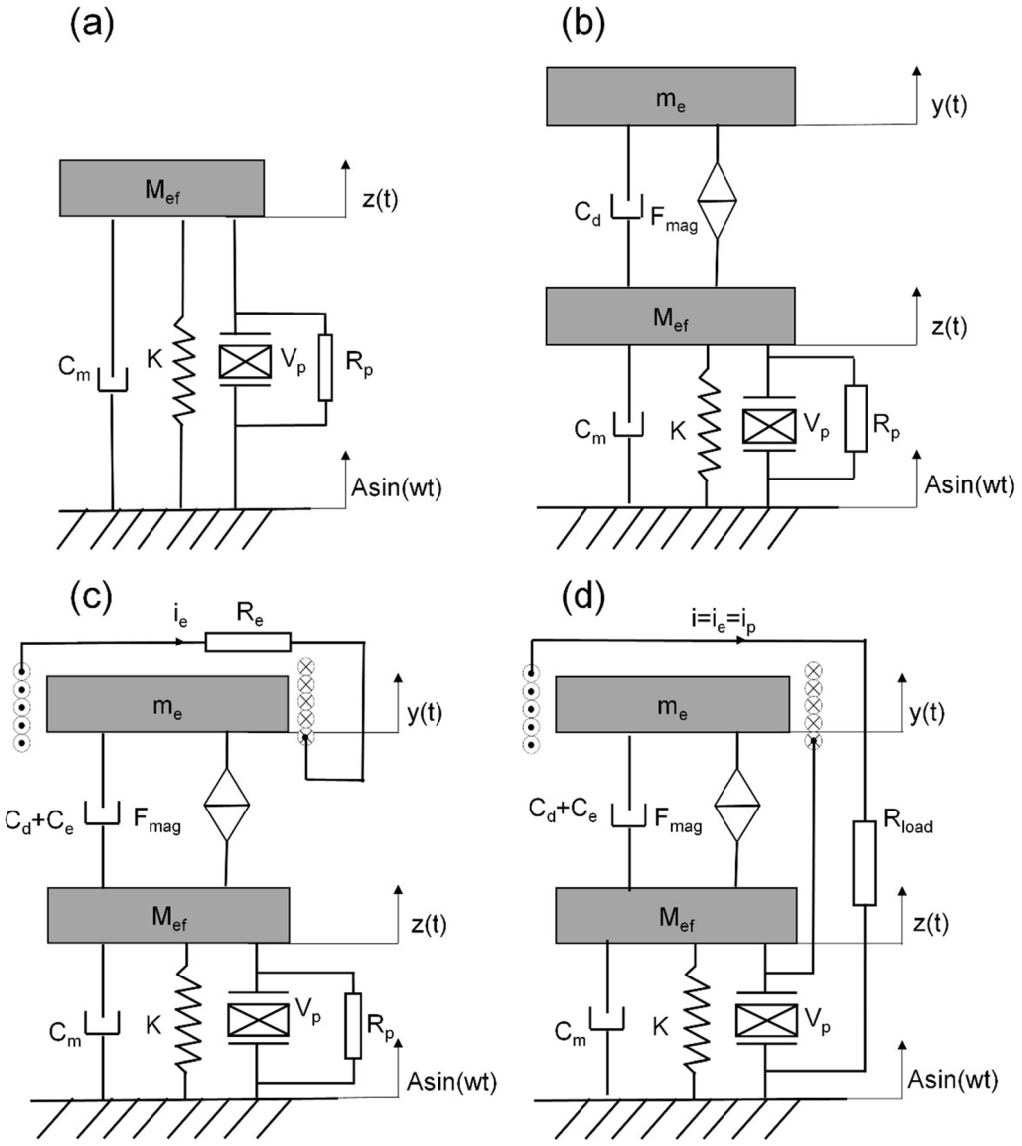

Fig. S1 Lumped-parameter representations of the studied HEHPE: (a) connection topology 1, (b) connection topology 2, (c) connection topology 3, and (d) connection topology 4

As for the HEHPE with connection topology 2, as shown in **Fig. S1**b, it can be treated as a nonlinear magnetic oscillator connected to the free end of the piezoelectric cantilever beam. The resulting lumped-parameter model is

$$\begin{aligned} M_{ef}\ddot{z} + C_m\dot{z} + Kz + \theta V_p - F_{mag} &= -M_{ef}A\sin(wt) \\ m_e\ddot{y} + C_d\dot{y} + F_{mag} &= -m_e\ddot{z} \\ C_p\dot{V}_p + \frac{V_p}{2R_p} - \theta\dot{z} &= 0 \end{aligned} \tag{S2}$$

in which F_{mag} is the nonlinear magnetic force between the moving magnet and the fixed magnet. It is dependent upon the displacement y of the moving magnet and the structural parameters of the electromagnetic part.

When it comes to connection topology 3, as shown in Fig. S1c, the external resistances R_e and R_p are independent upon each other, and the lumped-parameter model is

$$\begin{aligned} M_{ef}\ddot{z}+C_m\dot{z}+Kz+\theta V_p-F_{mag}&=-M_{ef}A\sin(wt)\\ m_e\ddot{y}+(C_d+C_e)\dot{y}+F_{mag}&=-m_e\ddot{z}\\ C_p\dot{V}_p+\frac{V_p}{2R_p}-\theta\dot{z}&=0 \end{aligned} \tag{S3}$$

It should be noted that, according to the classical electromagnetic theory, voltage across the induction coil can be expressed as (Nguyen et al., 2020.)

$$V_e=\frac{R_eND^2V_m\dot{y}}{h_{coil}(R_e+R_c)}\left(\frac{1}{((h_{coil}-2y)^2+D^2)^{\frac{3}{2}}}-\frac{1}{((h_{coil}+2y)^2+D^2)^{\frac{3}{2}}}\right). \tag{S4}$$

Here, N, D, h_{coil}, and R_c are the number of turns, diameter, thickness and internal resistance of the induction coil, respectively.

As shown in **Fig. S1**d, the connection topology 4 takes into account the electrically serial connection between the piezoelectric part and electromagnetic part. Considering an external load resistance of R_{load}, the following lumped-parameter model is formulated:

$$\begin{aligned} M_{ef}\ddot{z}+C_m\dot{z}+Kz+\theta V_p-F_{mag}&=-M_{ef}A\sin(wt)\\ m_e\ddot{y}+(C_d+C_e)\dot{y}+F_{mag}&=-m_e\ddot{z}\\ i&=2\left(\theta\dot{z}-C_p\dot{V}\right)\\ V_e&=\sigma\dot{y}-i\mathrm{R}_e-L_c\frac{di}{dt}\\ V_e+V_p&=iR_{load} \end{aligned} \tag{S5}$$

where i denotes the current flowing through the external resistance R_{load}, and σ is the electromechanical coupling coefficient for the electromagnetic part. Further, L_c can be obtained using the Wheeler formula (Wheeler et al., 1928)

$$L_c=\frac{7.875\times10^{-6}D_m^2N^2}{3D_m+9h_{coil}+5(D-d_0)} \tag{S6}$$

where $D_m=(D+d_0)/2$ is the average diameter of the coil.

S1.1 Magnetic force and the electromagnetic damping

To explicitly describe the magnetic force F_{mag} in the system, schematic diagram of electromagnetic part is shown in Fig. S2 (a) with dimensions explicitly designated. According to the Taylor expansion approximation by Nguyen et al., 2020 the magnetic force F_{mag} is expressed

with respect to the displacement y of the moving magnet as

$$F_{mag} = -(k_1 y + k_3 y^3) \tag{S7}$$

where k_1 and k_3 are the linear and nonlinear coefficients of magnetic force respectively, and their expressions are as follows:

$$\begin{aligned} k_1 = \frac{12\mathcal{B}_{fix}\mathcal{B}_m V_m}{\mu_0}\Bigg\{ & \frac{r^2(h-H)}{(r^2+(h-H)^2)^{\frac{5}{2}}} + \frac{r^2(h+H)}{(r^2+(h+H)^2)^{\frac{5}{2}}} \\ & - \frac{R^2(h-H)}{(R^2+(h-H)^2)^{\frac{5}{2}}} - \frac{R^2(h+H)}{(R^2+(h+H)^2)^{\frac{5}{2}}}\Bigg\} \end{aligned} \tag{S8}$$

$$\begin{aligned} k_3 = \frac{40\mathcal{B}_{fix}\mathcal{B}_m V_m}{\mu_0}\Bigg\{ & \frac{R^2(h+H)\,(3R^2-4(h+H)^2)}{(R^2+(h+H)^2)^{\frac{9}{2}}} - \frac{R^2(h-H)\,(3R^2-4(h-H)^2)}{(R^2+(h-H)^2)^{\frac{9}{2}}} \\ & - \frac{r^2(h-H)\,(3r^2-4(h-H)^2)}{(r^2+(h-H)^2)^{\frac{9}{2}}} - \frac{r^2(h+H)\,(3r^2-4(h+H)^2)}{(r^2+(h+H)^2)^{\frac{9}{2}}}\Bigg\} \end{aligned} \tag{S9}$$

where $\mathcal{B}_{fix}$ is the residual magnetic flux densities of the upper and lower fixed magnets, h and H are the height and the distance between the upper and lower fixed magnets respectively. $\mathcal{B}_m$ and V_m are the residual magnetic flux density and volume of the moving magnet, respectively. And $V_m = \pi h_m (R^2 - r^2)/4$, where R and r are the outer diameter and inner diameter of the ring magnet respectively. $\mu_0 = 4\pi \times 10^{-7} H/m$ is the magnetic permeability of a vacuum.

A series of computational analyses are also done to investigate the variation of magnetic forces, as shown in Fig. S2 (b). The computationally obtained relations between magnetic force F_{mag} and relative displacement y of the moving magnet is compared with the analytical formulations used above and plotted in Fig. S2 (c). It can be concluded that for a small relative displacement $y \leq 10$ mm, the analytical formulations show high accuracy of approximation.

Next, the influence of the distance H between the upper and lower fixed magnets upon magnetic force F_{mag} is computationally analyzed and the results are shown in Fig. S2 (d). It can be found that with the increase of H, the nonlinear dependence of F_{mag} upon y becomes weaker in the considered range $y \leq 30$ mm. That is to say, F_{mag} tends to be approximately proportional to y.

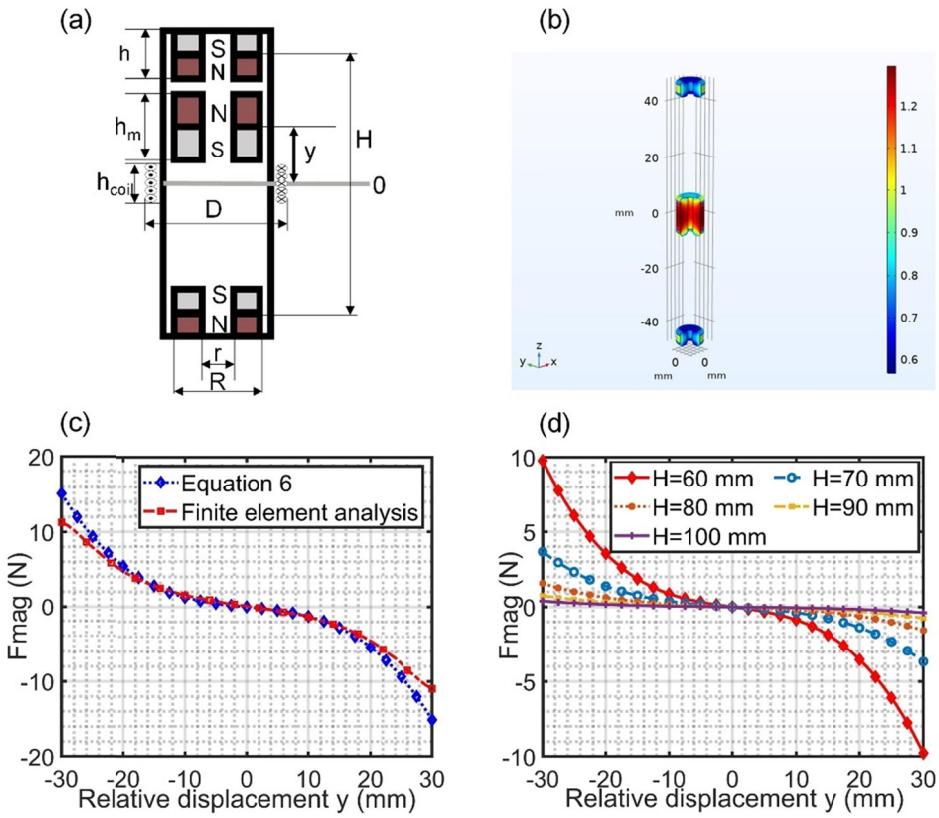

Fig. S2 Magnetic forces between the magnets: (a) schematic diagram of the electromagnetic part, (b) results from finite element simulation, (c) magnetic force obtained by finite element simulation compared with those obtained by Eq. (S7); (d) influence of the distance H on the dependence of F_{mag} over y according to Eq. (S7)

When electromagnetic part of the HEHPE is connected to a resistance load, a closed loop is formed. There will be current induced in the coil and then the moving magnet is subject to another force, called the electromagnetic damping force F_e. The force Fe is principally proportional to the relative velocity $\dot{y}$ of the moving magnet by $F_e = C_e \dot{y}$. The coefficient C_e, or the electromagnetic damping, is expressed by (Nguyen et al., 2020.)

$$C_e = \frac{D^4 \mathcal{B}_m^2 V_m^2 N^2}{h_{coil}^2 (R_c + \mathrm{R}_e)} \left(\frac{1}{(D^2 + (h_{coil} + 2y)^2)^{\frac{3}{2}}} - \frac{1}{(D^2 + (h_{coil} - 2y)^2)^{\frac{3}{2}}} \right) \tag{S10}$$

An example dependence curve of the electromagnetic damping C_e upon the relative displacement y of the moving magnet obtained from Eq. (S10) is shown in Fig. S3 a. It is seen that the initial zero-displacement point is a local minimum for the value of C_e. Meanwhile, two local maximum peaks are present when the moving magnet is totally outside the scope of the induction coil. To simplify the model, the maximum value of C_e, or C_{em}, is used exclusively to represent the electromagnetic damping in our derived model. With the number of turns N of the induction coil unchanged, thickness h_{coil} and outer diameter D of the induction coil vary

between 10 mm and 30 mm, respectively. The obtained values of C_e are shown with respect to relative displacement y of the moving magnet in Figs. S3c and S3d, respectively. The resulting values of C_{em} are shown in terms of the values of h_{coil} and D in Fig. S3b. Third-order polynomials are used to fit the relations with the detailed fitting expressions

$$y = -5.6\times10^{-6}h_{coil}^3 + 5.6057\times10^{-4}h_{coil}^2 - 0.0204h_{coil} + 0.2881 \tag{S11}$$

$$y = -3.9267\times10^{-5}D^3 + 0.0029D^2 - 0.0752D + 0.6772. \tag{S12}$$

The fitted relations are also plotted in Fig. S3b and compared with analytical results from Eq. (S10). Good agreement is found. What's more, it can be concluded that in the considered parameter ranges, h_{coil} shows a larger effect upon C_{em} than D. As it indicates, to achieve smaller electromagnetic damping, thinner induction coil is preferred.

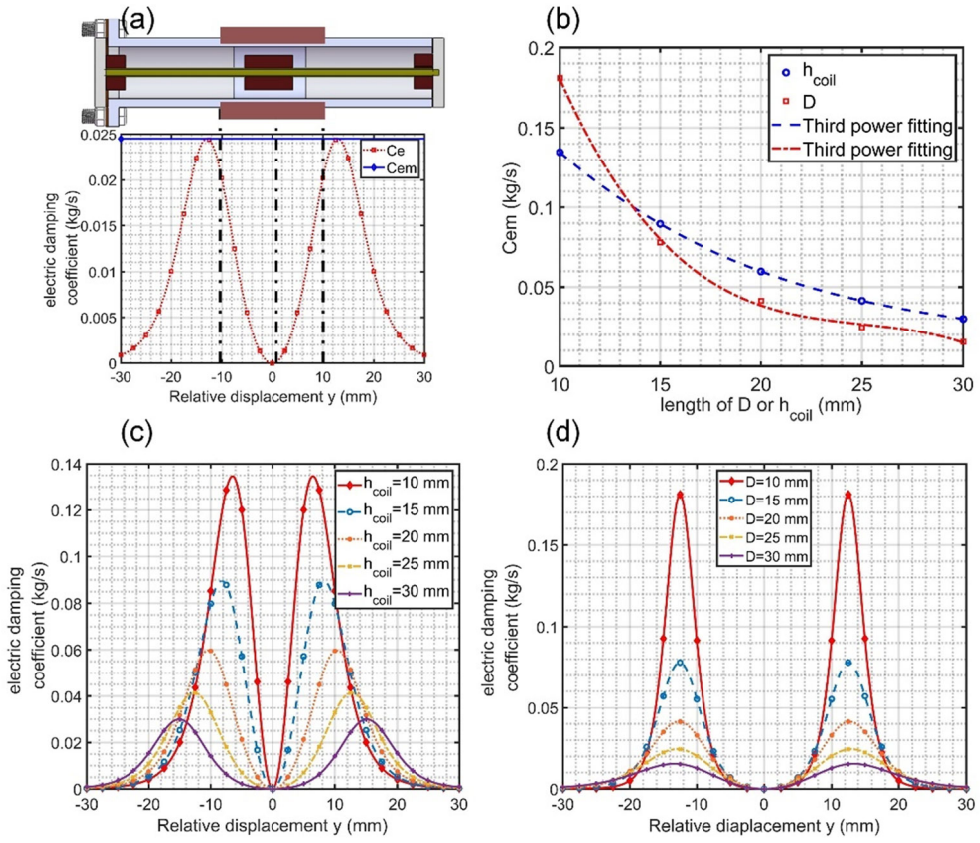

Fig. S3 (a) Electromagnetic damping C_e as a function of relative displacement y of the moving magnet; (b) Influence of h_{coil} and D upon C_{em} and the corresponding fitted approximations; (c) C_e as a function of y influenced by h_{coil}; (d) C_e as a function of y influenced by D

S1.2 Dimensionless analysis

For the convenience of analysis, the following dimensionless scheme is used:

$$z = h\overline{z},\ \ y = h\overline{y},\ \ V_p = \frac{\theta h}{C_p}\overline{V}_p,\ \ t = \frac{1}{w_n}\tau \tag{S13}$$

Where $\overline{z}$, $\overline{y}$, $\overline{V}_p$, and τ are dimensionless piezoelectric deflection, dimensionless displacement of the moving magnet, dimensionless voltage, and dimensionless time, respectively. h is the length scale, which is taken as the thickness of the fixed ring magnet. w_n is the natural frequency, which is taken as the first-order natural frequency of the piezoelectric cantilever beam. θ is the electromechanical coupling coefficient of the piezoelectric part of the HEHPE. C_p is the equivalent capacitance of piezoelectric ceramic plates.

Using the above dimensionless scheme (S13), governing equations of the studied HEHPE in connection topology 1 is reformulated into:

$$\begin{aligned} \ddot{\overline{z}} + 2\xi_m \dot{\overline{z}} + \overline{z} + \frac{\theta^2}{C_p w_n^2}\overline{V}_p &= -\frac{A}{h}\Omega\sin(\Omega\tau) \\ \dot{\overline{V}}_p + \frac{1}{2R_p C_p w_n}\overline{V}_p - \dot{\overline{z}} &= 0 \end{aligned} \tag{S14}$$

Where damping ratio $\xi_m = \frac{C_m}{2w_n}$, and $\Omega = \frac{w}{w_n}$.

The equations for connection topology 2 is then changed into:

$$\begin{aligned} \ddot{\overline{z}} + 2\xi_m \dot{\overline{z}} + \overline{z} + \frac{\theta^2}{C_p w_n^2}\overline{V}_p - \frac{k_1}{m_e w_n^2}\overline{y} - \frac{k_3}{m_e w_n^2}\overline{y}^3 &= -\frac{A}{h}\Omega\sin(\Omega\tau) \\ \ddot{\overline{y}} + \frac{C_e}{m_e w_n \dot{\overline{y}}} + \frac{k_1}{m_e w_n^2}\overline{y} + \frac{k_3}{m_e w_n^2}\overline{y}^3 &= -\ddot{\overline{z}} \\ \dot{\overline{V}}_p + \frac{1}{2R_p C_p w_n}\overline{V}_p - \dot{\overline{z}} &= 0 \end{aligned} \tag{S15}$$

The equations for connection topology 3 is converted into the form

$$\begin{aligned} \ddot{\overline{z}} + 2\xi_m \dot{\overline{z}} + \overline{z} + \frac{\theta^2}{C_p w_n^2}\overline{V}_p - \frac{k_1}{m_e w_n^2}\overline{y} - \frac{k_3}{m_e w_n^2}\overline{y}^3 &= \frac{A}{h}\Omega\sin(\Omega\tau) \\ \ddot{\overline{y}} + \frac{C_e + C_{em}}{m_e w_n \dot{\overline{y}}} + \frac{k_1}{m_e w_n^2}\overline{y} + \frac{k_3}{m_e w_n^2}\overline{y}^3 &= \ddot{\overline{z}} \\ \dot{\overline{V}}_p + \frac{1}{2R_p C_p w_n}\overline{V}_p - \dot{\overline{z}} &= 0 \end{aligned} \tag{S16}$$

The equations for connection topology 4 leads to

$$\begin{aligned} \ddot{\overline{z}} + 2\xi_m \dot{\overline{z}} + \overline{z} + \frac{\theta^2}{C_p w_n^2}\overline{V}_p - \frac{k_1}{M_{ef} w_n^2}\overline{y} - \frac{k_3}{M_{ef} w_n^2}\overline{y}^3 &= \frac{A}{h}\Omega\sin(\Omega\tau) \\ \ddot{\overline{y}} + \frac{C_e + C_d}{m_e w_n \dot{\overline{y}}} + \frac{k_1}{m_e w_n^2}\overline{y} + \frac{k_3}{m_e w_n^2}\overline{y}^3 &= \ddot{\overline{z}} \\ \ddot{\overline{V}}_p - \frac{(R_{load} + R_c)}{L_c w_n}\left(\dot{\overline{z}} - \dot{\overline{V}}_p\right) + \frac{1}{2L_c C_p w_n^2}\overline{V}_p + \frac{\sigma}{2L_c w_n}\overline{y} - \ddot{\overline{z}} &= 0 \end{aligned} \tag{S17}$$

S2 Analysis of the input and output signals

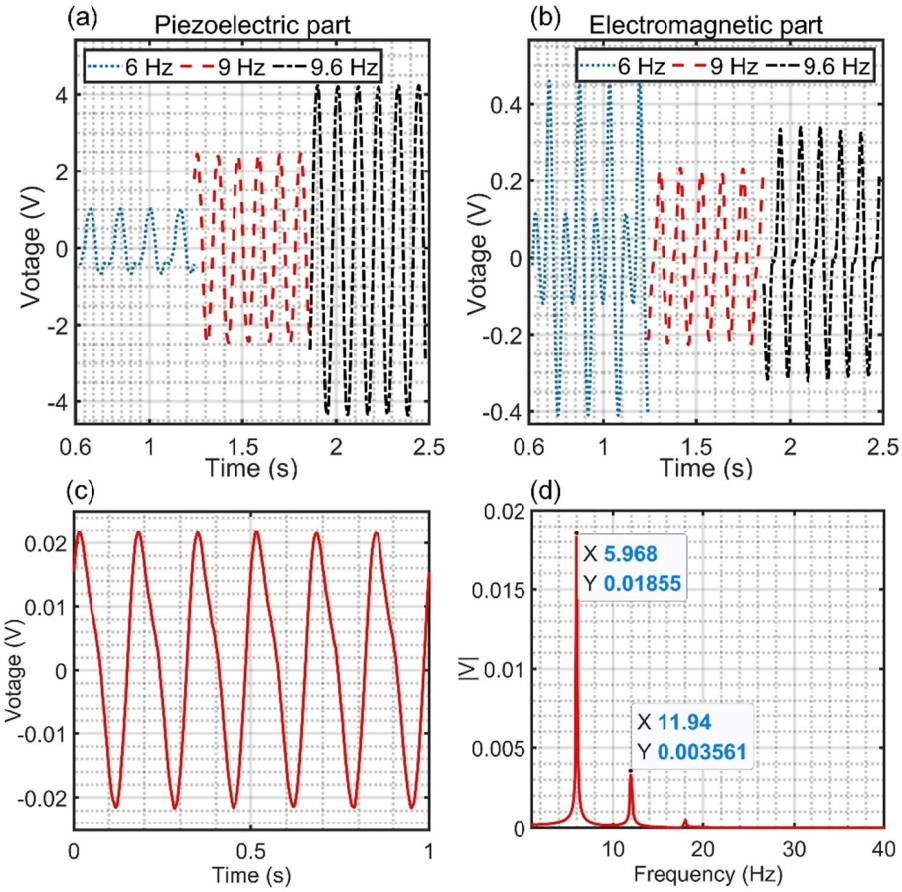

Fig. S4 Time-history voltage output of the HEHPE at different frequencies in connection topology 3: (a) the piezoelectric part and (b) the electromagnetic part. Voltage output of the acceleration sensor attached to the base of the HEHPE: (a) time-history signals and frequency spectrum

With connection topology 3, the HEHPE is excited with a base acceleration signal of an amplitude of 0.2 g. The load resistance connected to the piezoelectric part is set to be 70 kΩ, the load resistance Re connected to the electromagnetic part is set to be 150 Ω. Example time history of the voltage outputs of the piezoelectric part and the electromagnetic part in the studied HEHPE at different excitation frequencies are shown in **Fig. S4** (a) and (b), respectively.

It is seen from **Fig. S4** (a) that at the base excitation frequency of 9 Hz and 9.6 Hz, output voltage of the piezoelectric part assumes a good sinusoidal waveform, while at base excitation frequency of 6 *Hz*, the voltage output waveform is of multifrequency components. For the electromagnetic part, however, the output voltage waveform is not purely sinusoidal in the considered frequency range, as shown in **Fig. S4** (a). This leads us to double check the output

acceleration of the vibration exciter. To this end, input signal to the vibration exciter is set to be of sinusoidal waveform at the frequency of 6 Hz, output vibration acceleration of the base is then recorded using an acceleration sensor and plotted in **Fig. S4** (c) with corresponding frequency spectrum shown in **Fig. S4** (d). It is obviously shown that though of relatively small amplitude, the output signal of the vibration exciter is not of single frequency component. The higher frequency components of the excited acceleration signal can not be neglected. In fact, the output vibration signals contain frequency components of 5.968 Hz and 11.94 Hz together. Note that these values do not strictly correspond to the frequency 6 Hz given by the signal generator. This may be caused by system error and can be ignored in our situation.

Therefore, both the input and output of the studied HEHPE contain multifrequency components. This feature brings into question the usual method of characterization of the output performance of the studied HEHPE. In fact, it is currently widely adopted that the output performance of an energy harvester, say, amplitude of output voltage, is plotted against base excitation frequency, whose trend is checked to extract the resonant frequency and maximized output voltage. Two points are to be concerned. Firstly, due to the multi-frequency nature, the "amplitude" measuring the difference between the maximum value and minimum value of the output signal is not an appropriate indicator. Secondly, in the frequency amplitude plot, each point should corresponding to a single frequency component. Therefore, in the treatment of experimental results, we have to take care of the frequency components of the output signal before resorting to any data processing and performance evaluation.

With an acceleration amplitude of 0.2 g, a base excitation of 6.4 Hz is applied to the HEHPE in connection topology 3. The resulting time-history output voltage from the piezoelectric part is shown in **Fig. S5** (a). Obviously, the signal contains high frequency noise, which can be filtered and leads to the signal shown in **Fig. S5** (b) with blue hollow circles. Frequency spectrum of the filtered signal is shown in **Fig. S5** (c), from which we can easily identified many higher-order harmonics, though the calculated base frequency is around 6.452 Hz, instead of exactly 6.4 Hz.

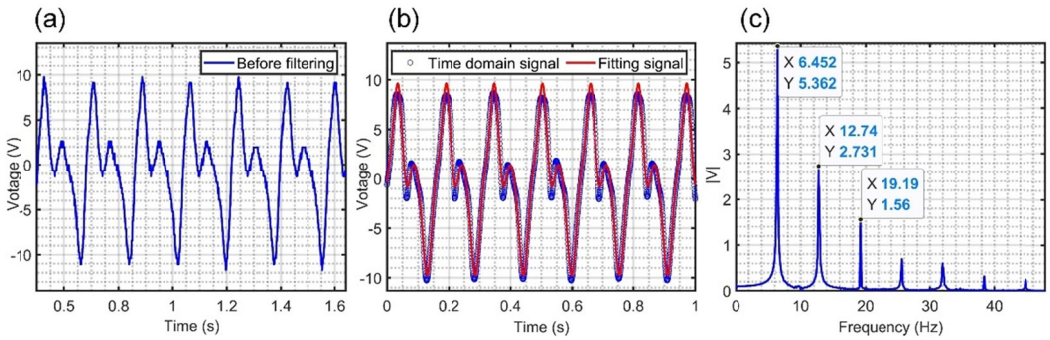

Fig. S5 Output voltage of the piezoelectric part in connection topology 3 under the excitation frequency of 6.4 Hz: (a) time-history voltage, (b) filtered and fitted voltages, and (c) frequency spectrum of filtered voltages

From **Fig. S5** (c), it is known that harmonics higher than third-order are of relatively small amplitude. Thus, we use the following fitting equations based on Fourier series to approximate the time-history signal

$$F_{fit} = A_0 + A_1 \sin(2\pi f_0 t + \phi_1) + A_2 \sin(4\pi f_0 t + \phi_2) + A_3 \sin(6\pi f_0 t + \phi_3) + \ldots \tag{S18}$$

where A_i and ϕ_i represent the magnitude and phase angle of given harmonics, respectively, f_0 denotes the base frequency, i = 1, 2, 3, $\cdots$.

Setting the base frequency = 6.4 Hz, the fitted results are shown in **Fig. S5** (b) with red solid lines. According to the calculations, amplitude of the first-order harmonic is 6.407 V, while amplitudes of the second-order and third-order harmonics are, 3.436 V and 1.555 V, respectively. These results do not coincide with the signal spectrum shown in **Fig. S5** (c). Therefore, it is recommended that Fourier series fitting instead of direct Fourier transform should be used to extract the frequency components in a given signal in our situation.

The same procedures are applied to the analysis of acceleration signal provided by the vibration exciter. The results are shown in **Fig. S6**. Similarly, the base excitation frequency is set to be 6.4 Hz. Note that the signal considered here is relatively pure sinusoidal and does not need filtering. Since the sensitivity of acceleration sensor is 100.08 mV/g, the time domain signal shown in **Fig. S6** (a) implies a voltage amplitude of around 0.02 V, and the corresponding acceleration is around 0.2 g. Amplitudes for the first three harmonics are 0.01975 V, 0.004246 V, and 0.000692 V, respectively.

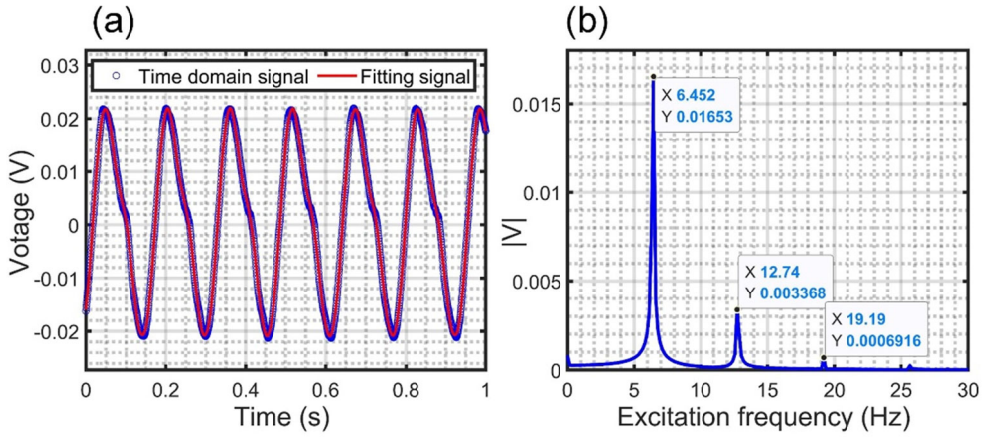

Fig. S6 Output voltage of the acceleration sensor attached to the base of the HEHPE at the base excitation frequency of 6.4 Hz: (a) original and fitted time-history voltages, and (b) frequency spectrum of the voltage signal

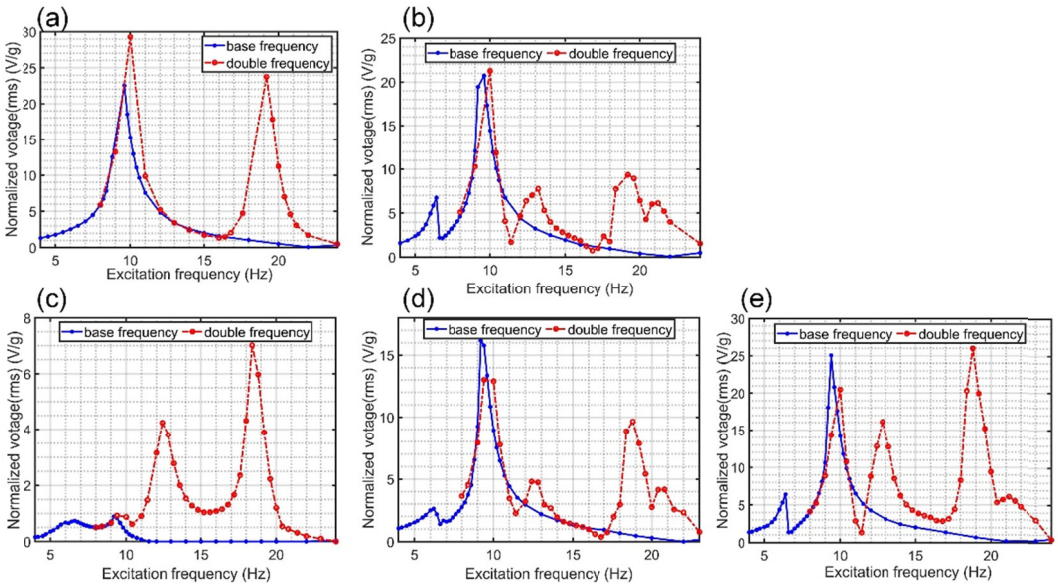

Fig. S7 (a) Frequency response of the HEHPE with connection topology 1; (b) Frequency response of the HEHPE with connection topology 2; Frequency responses of the piezoelectric part (c) and the electromagnetic part (d) for connection topology 3; (e) Frequency response of the HEHPE with connection topology 4. The "base frequency" and "double frequency" here corresponds to the first-order and second-order harmonics obtained in (18), respectively

With the above described procedures for the input and output signals of the studied HEHPE, the remaining question is how to measure the performance of HEHPE. Due to the nonlinearity in HEHPE, multi-frequency input and output signals are commonly obtained in the experiments. A quasi-linear process is established. We extract the first two harmonics shown in the Fourier series fitting of given signals. After that, for a given set of experimentally obtained input and output

signals, we correspond the amplitudes of the same order of harmonics in the fitted input and output signals. They ratios between the output and input amplitudes are then plotted against frequency of the underlying harmonics, as shown in **Fig. S7**. The results in terms of four connection topologies are simultaneously shown. As a comparison, the results which contain only the first harmonic are also shown.

It is clearly shown in **Fig. S7** that in the low frequency range (f smaller than 12 Hz or so), the curve for the second harmonic coincides with that for the first-order harmonics. In the meantime, for the relatively high frequency range (f greater than 12 Hz or so), the two curves deviate from each other. This phenomenon partly validate our assumption of quasi-linearity. Also, it indicates that nonlinearity in the system begins to come into play when base excitation frequency surpasses a certain limit. From a practical perspective of view, extraction of higher-order harmonics is useful in the investigation of dynamical behavior of the system.

References

Nguyen, H.T., Genov, D.A., Bardaweel, H., 2020. Vibration energy harvesting using magnetic spring based nonlinear oscillators: Design strategies and insights. Applied Energy 269, 115102. https://doi.org/10.1016/j.apenergy.2020.115102

Wheeler, H.A., 1928. Simple inductance formulas for radio coils. Proceedings of the institute of Radio Engineers 16(10), 1398–1400. https://doi.org/10.1109/JRPROC.1928.221309